



Dwell fatigue crack nucleation model based on crystal plasticity finite element simulations of polycrystalline titanium alloys

Masoud Anahid ^a, Mahendra K. Samal ^a, Somnath Ghosh ^{b,*}

^a Department of Mechanical Engineering, The Ohio State University, 201 West 19th Avenue, Columbus, OH 43210, USA

^b Department of Civil Engineering, Johns Hopkins University, 203 Latrobe, 3400 N. Charles Street, Baltimore, MD 21218, USA

ARTICLE INFO

Article history:

Received 30 November 2010

Received in revised form

8 May 2011

Accepted 14 May 2011

Available online 23 May 2011

Keywords:

Fatigue crack nucleation

Crystal plasticity

Load shedding

Titanium alloys

Dislocation pileup

ABSTRACT

In this paper a crystal plasticity-based crack nucleation model is developed for polycrystalline microstructures undergoing cyclic dwell loading. The fatigue crack nucleation model is developed for dual-phase titanium alloys admitting room temperature creep phenomenon. It is a non-local model that accounts for the cumulative effect of slip on multiple slip systems, and involves evolving mixed-mode stresses in the grain along with dislocation pileups in contiguous grains. Rate dependent, highly anisotropic behavior causes significant localized stress concentration that increases with loading cycles. The crystal plasticity finite element (CPFE) model uses rate and size-dependent anisotropic elasto-crystal plasticity constitutive model to account for these effects. Stress rise in the hard grain is a consequence of time-dependent load shedding in adjacent soft grains, and is the main cause of crack nucleation in the polycrystalline titanium microstructure. CPFE simulation results are post-processed to provide inputs to the crack nucleation model. The nucleation model is calibrated and satisfactorily validated using data available from acoustic microscopy experiments for monitoring crack evolution in dwell fatigue experiments.

© 2011 Elsevier Ltd. All rights reserved.

1. Introduction

Titanium alloys with predominantly hexagonal close-packed (*hcp*) crystalline structure are used in various high performance automotive and aerospace propulsion applications due to their high strength (~ 700 – 1000 MPa), low density, high fracture toughness and corrosion resistance. However, the performance of Ti alloys is often hindered by time-dependent deformation at temperatures that are lower than those at which diffusion-mediated deformation, such as dislocation climb, occurs. This deformation characteristic leads to their premature fatigue failure under dwell loading service conditions (Bache, 2003). Each dwell loading cycle is comprised of a loading phase followed by a hold phase, and subsequently an unloading phase. Crack nucleation under these conditions has been experimentally associated with grains that have their [0 0 0 1] crystal orientations ($\langle c \rangle$ -axis) close to the deformation axis (Sinha et al., 2006a). This early failure, in comparison with normal fatigue without any hold, has been attributed to local creep effects that occur during the hold period of dwell, e.g. in Imam and Gilmore (1979), Kirane and Ghosh (2008), and Kirane et al. (2009).

Plastic deformation in *hcp* Ti alloys has considerable dependence on the crystal orientation due to their low symmetries (Hasija et al., 2003; Deka et al., 2006; Venkatramani et al., 2006). Slip behavior due to dislocation glide in hexagonal

* Corresponding author. Tel.: +1 410 516 7833; fax: +1 410 516 7473.

E-mail address: sghosh20@jhu.edu (S. Ghosh).

materials is highly anisotropic because of the difference in deformation resistances in different slip systems. The critical resolved shear strength (CRSS) for the $\langle c+a \rangle$ -slip on pyramidal planes is $\sim 3\text{--}4$ times larger than the CRSS for $\langle a \rangle$ -type slip on prism or basal planes. During the hold period, “soft” grains with favorably oriented $\langle a \rangle$ -type slip systems for dislocation glide ($\langle c \rangle$ -axis with nearly 45° orientation with respect to the deformation axis) undergo significant plastic straining. Contiguous “hard” grains with less-favorably oriented for $\langle a \rangle$ -type slip ($\langle c \rangle$ -axis parallel to the deformation direction), experience large local stress concentrations, especially near the shared grain boundary. This is a consequence of compatible, large elastic strains in the hard grains near the shared boundary. The phenomenon of rising stress-concentration with evolving creep strains in dwell cycles has been called load shedding in Hasija et al. (2003). This rise in local stresses is found to cause early crack nucleation under dwell fatigue loading in Bache (2003).

Fatigue failure in metallic materials due to cyclic loading evolves in multiple stages (Suresh, 1998). These include micro-crack nucleation due to inhomogeneous plastic flow or grain boundary failure, followed by crack growth due to cyclic stresses, and finally coalescence of cracks to cause fast crack propagation. Depending on the material in question, and other factors like geometry, surface condition, stress/strain amplitude, strain rate, environment, etc., the number of cycles to nucleation and the propagation can be quite different. For example, experimental investigations on dwell fatigue in Ti-6242 alloy in Rokhlin et al. (2005) using acoustic microscopy suggest that primary sub-surface crack nucleation occurs at $\sim 80\text{--}90\%$ of the total number of cycles to failure. These experiments show that nucleation can dominate the life limit of a metallic material. Consequently, fatigue crack nucleation has drawn considerable attention from the research community because of its role in catastrophic material failure.

A large body of literature exists on the prediction of fatigue life of metals. The phenomena of high cycle and low cycle fatigue have been traditionally characterized using macroscopic parameters like applied stresses, cyclic frequency, loading waveform, hold time, etc., as well as statistical distributions of fatigue life and fatigue strength (Suresh, 1998; Coffin, 1973; Laird, 1976; Fleck et al., 1994; Hashimoto and Pereira, 1996). Fatigue analysis by total life approaches includes (i) the stress-life or S-N approach, where the stress amplitude versus life is determined, and (ii) the strain-life approach e.g. the Coffin–Manson rule, where the number of cycles to failure is determined as a function of plastic strain. However, predictions of these widely used models can suffer from significant scatter. This is primarily due to the absence of robust underlying physical mechanisms and information on the material microstructure in their representation. Morphological and crystallographic characteristics of the microstructure, e.g. crystal orientations, misorientations and grain size distribution, play significant roles in the mechanical behavior and fatigue failure response.

A number of models have also been proposed for fatigue crack nucleation. Some of the early models are based on the phenomenon of roughening of initially smooth surfaces with the application of cyclic stresses and strains in Fine and Ritchie (1979). More recent work on fatigue in polycrystalline materials (Kim and Laird, 1978a; Lim, 1987; Heinz and Neumann, 1990) postulates grain boundaries, which are critical to persistent slip bands in grains and free surfaces, as preferential sites of micro-crack nucleation and propagation. Inter-granular fatigue cracking has been investigated for the relation between grain boundary orientation and the direction of applied loading in Heinz and Neumann (1990). Micro-crack nucleation due to grain boundary interaction with persistent slip bands has been studied in Zhang and Wang (2003). Inter-granular fatigue crack nucleation is predominant at sites with large misorientation between adjacent grains (Kim and Laird, 1978b). The nucleation of a fatigue crack has been attributed to random fluctuations in a metastable assembly of defect structures generated during cyclic deformation in Lin et al. (1986). A micro-crack nucleates when the Gibbs free energy changes due to the applied loading as well as other participating mechanisms, e.g. evolution of lattice defects overcomes the energy barrier for creating new surfaces. This model has been used in Yao et al. (2007) to predict the number of cycles for micro-crack nucleation in steel and aluminum alloys. Another class of fatigue crack nucleation models based on the void growth in a plastically deforming matrix has been proposed (Rice and Tracey, 1969). Accumulated plastic strain has been used as a fatigue indicator parameter to predict fatigue crack nucleation site in materials which experience cracking within a band of intense slip. In McDowell and Dunne (2010), it is shown that the experimentally observed cracking in a polycrystalline Ni-based superalloy sample occurs in regions with the highest accumulated plastic strain predicted by the crystal plasticity simulations. A cleavage fracture criterion based on the stress normal to the basal plane has been introduced for Ti alloys to predict the features of crack formation site in Dunne and Rugg (2008) and McDowell and Dunne (2010). Using a crystal plasticity model along with this cleavage failure criterion, it has been shown that facets nucleate along the basal plane of a hard grain which has neighboring grains with very specific orientations. This combination has been termed a rogue grain combination.

The recent years have seen a paradigm shift towards the use of material microstructure-based detailed mechanistic models for predicting fatigue crack nucleation and propagation. The mechanistic models are promising alternatives to the empirical models. A review of some of the existing physics-based failure models is presented in Ghosh et al. (2010). Many of the microstructure-based fatigue models seek accurate description of material behavior through crystal plasticity-based finite element models. Crystal plasticity theories with explicit grain structures are effective in predicting localized cyclic plastic strains (Mineur et al., 2000; Bennett and McDowell, 2003; Chu et al., 2001). The mechanical behavior of aluminum alloys under cyclic loading has been studied using CPFE simulations of crystalline aggregates in Turkmen et al. (2003) and Dawson (2000). Crystal plasticity modeling with kinematic hardening for fatigue loading of Ti-6Al-4V has been presented in Morrissey et al. (2003) and Goh et al. (2003, 2006). Crystal plasticity models for deformation and ratcheting fatigue of HSLA steels have been developed in Xie et al. (2004) and Sinha and Ghosh (2006). Ghosh et al. have developed experimentally validated, size-dependent crystal plasticity FE models for titanium alloys in Hasija et al. (2003),

Deka et al. (2006), Venkatramani et al. (2006), and Venkataramani et al. (2007), especially for modeling the load shedding phenomenon.

An early version of dwell fatigue crack nucleation model was developed in Kirane and Ghosh (2008) and Kirane et al. (2009) from CPFE simulations. This model capitalizes on the similarities between crack evolution at the tip of a crack and a dislocation pileup to derive a non-local crack nucleation criterion. However a limiting assumption made in this model is that dislocation pileup in neighboring soft grains follows the same distribution function as for single slip. However, the dislocation density distribution function per unit length is based on single slip activity, while the total dislocation density per unit area is a cumulative effect of slip on multiple slip systems. This inconsistency can lead to significant inaccuracies in the prediction of dwell fatigue crack nucleation.

The present paper overcomes the limitations of the model in Kirane and Ghosh (2008) and Kirane et al. (2009) by avoiding the assumptions. It develops an experimentally validated, microstructure-based crack nucleation model for polycrystalline titanium alloys subject to cyclic dwell loading conditions. This non-local model accounts for the cumulative effect of slip on multiple slip systems, and involves evolving mixed-mode stresses in the grain along with dislocation pileups in contiguous grains. The role of impurity inclusions on crack nucleation is ignored in this model. The paper starts with a brief description of the crystal plasticity finite element model for load shedding in polycrystalline microstructures in Section 2. Section 3 discusses experimental methods of fractography and acoustic microscopy used for crack monitoring in Rokhlin et al. (2005) and for validation of the nucleation model. A brief review of a few microstructure-based failure models is given in Section 4. Details of the computational procedure for evaluating the nucleation criterion are discussed in Section 5. Material constants in this criterion are calibrated using dwell fatigue simulation data at critical failure sites. Finally, the predictive capabilities of this model are demonstrated through a number of experimental validation tests in Section 6.

2. Crystal plasticity finite element (CPFE) model for dwell fatigue

Ti alloys are often characterized by time-dependent “cold” creep deformation characteristics at temperatures lower than those, at which diffusion-mediated deformation such as dislocation climb is expected (Imam and Gilmore, 1979; Neeraj et al., 2000; Hasija et al., 2003). TEM studies, e.g. in Neeraj et al. (2000) have shown that deformation actually proceeds via dislocation glide, and dislocations are inhomogeneously distributed into planar arrays. Significant creep strains can accumulate at applied stresses, even as low as 60% of the yield strength. This characteristic has been attributed to rate sensitivity effects in Imam and Gilmore (1979). The α/β forged Ti-6242, studied in this paper, is a biphasic polycrystalline alloy. It consists of colonies of transformed- β phase in a matrix of the primary α (*hcp*) phase. The primary α phase consists of equiaxed grains with an *hcp* structure, whereas the transformed- β colonies have alternating α (*hcp*) and β (*bcc*) laths. The alloy in this study consists of 70% primary α and 30% transformed- β grains. A size- and time-dependent large strain crystal plasticity-based FE model has been developed and experimentally validated in Hasija et al. (2003), Deka et al. (2006), Venkatramani et al. (2006), and Venkataramani et al. (2007, 2008). For the transformed β -phase colony regions, a homogenized equivalent crystal model is developed in Deka et al. (2006).

2.1. Crystal plasticity constitutive relations

The stress-strain relation is written in terms of the second Piola-Kirchoff stress \mathbf{S} and its work conjugate Lagrange-Green strain tensor \mathbf{E}^e as

$$\mathbf{S} = \mathbf{C} : \mathbf{E}^e \quad \text{where } \mathbf{E}^e = \frac{1}{2}(\mathbf{F}^e)^T \mathbf{F}^e - \mathbf{I} \quad (1)$$

\mathbf{C} is a fourth order anisotropic elasticity tensor and \mathbf{F}^e is the elastic component of the deformation gradient deformation gradient, obtained by multiplicative decomposition as

$$\mathbf{F} = \mathbf{F}^e \mathbf{F}^p, \quad \det(\mathbf{F}^e) > 0 \quad (2)$$

where \mathbf{F} is the deformation gradient tensor and \mathbf{F}^p is its incompressible plastic component, i.e. $\det \mathbf{F}^p = 1$. The plastic part of the crystal plasticity equations involves a combined effect of slip on multiple slip systems. The flow rule, governing evolution of plastic deformation, is expressed in terms of the plastic velocity gradient \mathbf{L}^p as

$$\mathbf{L}^p = \dot{\mathbf{F}}^p \mathbf{F}^{p-1} = \sum_{\alpha}^{nslip} \dot{\gamma}^{\alpha} \mathbf{s}^{\alpha} \quad (3)$$

where the Schmid tensor associated with α th slip system \mathbf{s}^{α} is expressed in terms of the slip direction \mathbf{m}_0^{α} and slip plane normal \mathbf{n}_0^{α} in the reference configuration as $\mathbf{s}^{\alpha} = \mathbf{m}_0^{\alpha} \otimes \mathbf{n}_0^{\alpha}$. The plastic slip rate $\dot{\gamma}^{\alpha}$ on the α th slip system has a power law dependence on the resolved shear stress (τ^{α}) and the slip system deformation resistance (g^{α}), given as

$$\dot{\gamma}^{\alpha} = \dot{\gamma} \left| \frac{\tau^{\alpha} - \chi^{\alpha}}{g^{\alpha}} \right|^{1/m} \text{sign}(\tau^{\alpha} - \chi^{\alpha}) \quad (4)$$

Here m is the material rate sensitivity parameter, $\dot{\gamma}$ is the reference plastic shearing rate and χ^α is the back stress that accounts for kinematic hardening in cyclic deformation (Hasija et al., 2003).

The evolution of slip system deformation resistance is assumed to be controlled by two types of dislocations, viz. statistically stored dislocations (SSDs) and geometrically necessary dislocations (GNDs). SSDs correspond to homogeneous plastic deformation, while GNDs accommodate incompatibility of the plastic strain field due to lattice curvature, especially near grain boundaries. The corresponding deformation resistance rate is expressed as

$$\dot{g}^\alpha = \sum_\beta h^{\alpha\beta} |\dot{\gamma}^\beta| + k_0 \frac{\dot{\alpha}^2 G^2 b}{2(g^\alpha - g_0^\alpha)} \sum_\beta \lambda^\beta |\dot{\gamma}^\beta| \quad (5)$$

The first term in Eq. (5) corresponds to SSDs. The modulus $h^{\alpha\beta} = q^{\alpha\beta} h^\beta$ (no sum on β) is the strain hardening rate due to self and latent hardening on the α th slip system by slip on the β th slip system respectively. Here, h^β is the self-hardening coefficient and $q^{\alpha\beta}$ is a matrix describing latent hardening. The second term in Eq. (5) accounts for the effect of GNDs on work hardening (Acharya and Beaudoin, 2000). Here, k_0 is a dimensionless material constant, G is the elastic shear modulus, b is the Burgers vector, g_0^α is the initial deformation resistance and $\dot{\alpha}$ is a non-dimensional constant. $\dot{\alpha}$ is taken to be $\frac{1}{3}$ in this work following (Ashby, 1970). λ^β is a measure of slip plane lattice incompatibility, which can be expressed for each slip system slip system as a function of slip plane normal \mathbf{n}^β and an incompatibility tensor Λ as

$$\lambda^\beta = (\Lambda \mathbf{n}^\beta : \Lambda \mathbf{n}^\beta)^{1/2} \quad (6)$$

The dislocation density tensor Λ , introduced in Nye (1953) is a direct measure of the GND density. It can be expressed using the curl of plastic deformation gradient tensor \mathbf{F}^P . Since this crystal plasticity formulation does not explicitly incorporate a dislocation density tensor, it is indirectly extracted from the CPFE output data as

$$\Lambda = \nabla^T \times \mathbf{F}^P \quad (7)$$

Grain size has a significant effect on the initial deformation resistance g_0^α . A Hall–Petch type relation with various slip direction-dependent characteristic length scales has been incorporated in the CPFE model in Venkataramani et al. (2007, 2008). Material properties for each constituent phase and individual slip system in the crystal plasticity model, as well as size effect parameters have been calibrated in Deka et al. (2006), Venkatramani et al. (2006, 2007). Other parameters used in Eq. (5) include (i) shear modulus $G=48$ GPa, (ii) magnitude of Burgers vector $b=0.30$ nm, and (iii) $k_0=2$. Details of the microstructural morphology are also accounted for in the CPFE model through accurate phase volume fractions and orientation distributions. Extensive developments on polycrystalline microstructures that are statistically equivalent to those observed in OIM scans have been made in Ghosh et al. (2008), Groeber et al. (2008a,b). The statistically equivalent polycrystalline models are used in this study for simulating real microstructures.

2.2. CPFE simulations of polycrystalline Ti-6242

CPFE simulations of polycrystalline Ti-6242 under dwell loading conditions are conducted for evaluating stress and strain fields, required for predicting crack nucleation. Results from these simulations are used in Section 6 to develop the proposed crack nucleation model. The crystal plasticity simulations follow dwell fatigue experiments in Rokhlin et al. (2005), which are to calibrate and validate the crack nucleation model. Experiments in Rokhlin et al. (2005) use three dog-bone specimens that are extracted from a Ti-6242 pancake forging provided by Ladish. The microstructure of these specimens have significant difference in crystallographic orientation, misorientation and micro-texture distribution. The dwell tests subject these specimens to cyclic loads with trapezoidal waveforms. Each load cycle has a maximum applied traction of 869 MPa ($\sim 95\%$ of the macroscopic yield stress for the overall material) at a hold time of 2 min, and a loading/unloading time of 1 s. The R -ratio, measured as the ratio of the minimum to maximum loading amplitudes, is zero.

Computer microstructures are reconstructed using methods developed in Ghosh et al. (2008) and Groeber et al. (2008a,b) from orientation imaging microscopy or OIM images at two sites in the material specimens. These are: (i) a critical microstructural region of a dwell fatigue crack tip and (ii) a non-critical region, where no cracks are observed microscopically. The OIM image for specimen 1 at the critical region is shown in Fig. 1. As discussed in Groeber et al. (2008a,b), statistical distribution functions of various microstructural parameters in the 2D OIM scan are generated and stereologically projected in the third dimension for creating the 3D statistics. The reconstructed 3D models have distributions of orientation, misorientation, microtexture, grain size and number of neighbors that are statistically equivalent to those observed experimentally in the OIM scans. Subsequently, CPFE models of the statistically equivalent microstructures are developed for analyzing the behavior of the critical and non-critical regions. A representative $65 \mu\text{m} \times 65 \mu\text{m} \times 65 \mu\text{m}$ microstructural volume element of specimen 1 (critical region) consisting of 949 grains is shown in Fig. 2(a).

Prior to accepting a mesh for CPFE simulation leading to crack nucleation, a convergence study is conducted to examine mesh sensitivity. The critical microstructure of specimen 1 is simulated with finite element models of two different mesh densities. The first model consists of 78 540 tetrahedron CST elements, while the second has 116 040 elements, which is approximately 150% higher in mesh density. A creep simulation is performed for both these models for 1000 s at an applied load of 869 MPa in the Y-direction. The local stress component in the loading direction and the local plastic strain

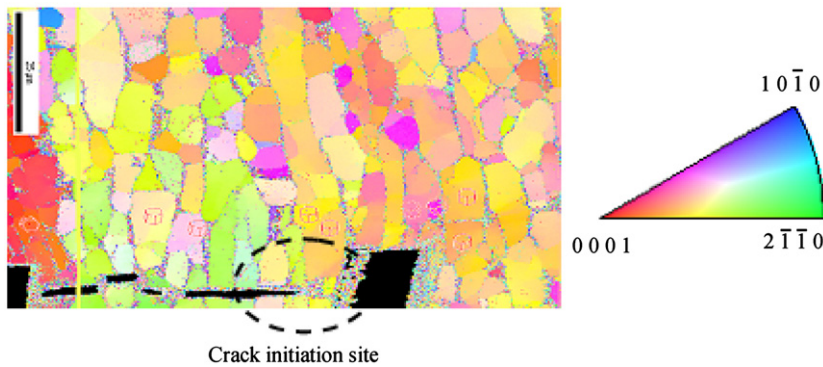


Fig. 1. OIM scan of the critical primary crack nucleation site in specimen 1 microstructure.

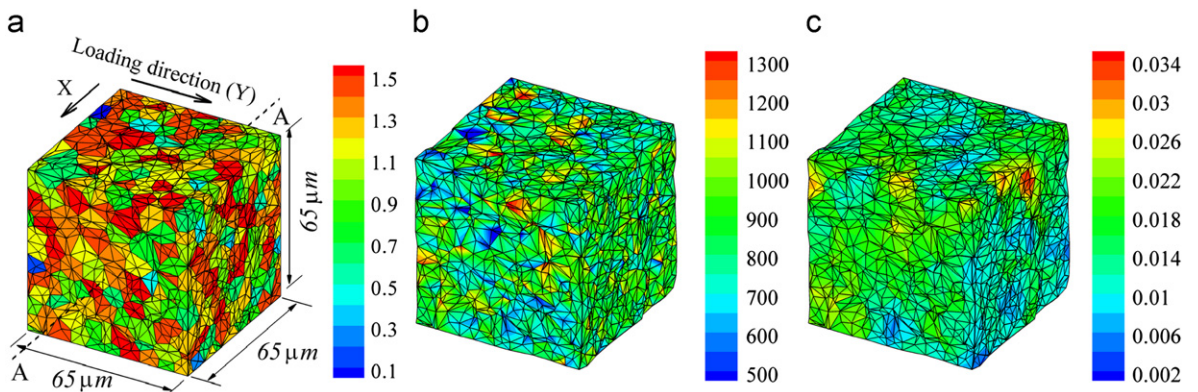


Fig. 2. (a) CPFE model of the statistically equivalent microstructure of polycrystalline Ti-6242 at a critical location of specimen 1 depicting c -axis orientation distribution contour (radians), (b) contour plot of loading direction stress σ_{22} , and (c) contour plot of loading direction plastic strain ε_{22}^p .

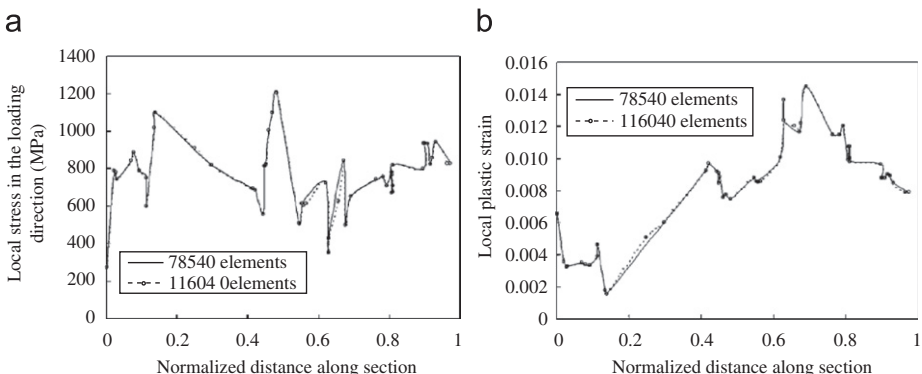


Fig. 3. Distribution of local variables: (a) loading direction stress (σ_{22}), (b) local plastic strain along a section parallel to the x -axis at the end of 1000 s for a creep simulation on the two models of critical microstructure of specimen 1 with two different mesh densities.

at the end of 1000 s are compared for various sections in the FE models. Plots comparing the distribution of these variables along a section parallel to the X -axis are shown in Fig. 3(a) and (b). The figures display excellent agreement between the two models with different mesh densities. It is concluded that the 78 540-element mesh is a converged model for the loading considered and is used for the development of the crack initiation criterion. The CPFE models of specimens 1, 2 and 3 are run for 352, 663 and 447 cycles respectively, which correspond to the observed number of cycles to failure in the experiments.

Figs. 2 and 4 depict the results of CPFE simulations for the model of specimen 1 located in the critical region. Fig. 2(b) and (c) shows the contour plots of the loading direction local stress (σ_{22}) and plastic strain ε_{22}^p respectively. Fig. 4(a) plots the local stress σ_{22} after 1 cycle and 300 cycles respectively along a section AA shown in Fig. 2(a). This section AA passes through a hard-soft

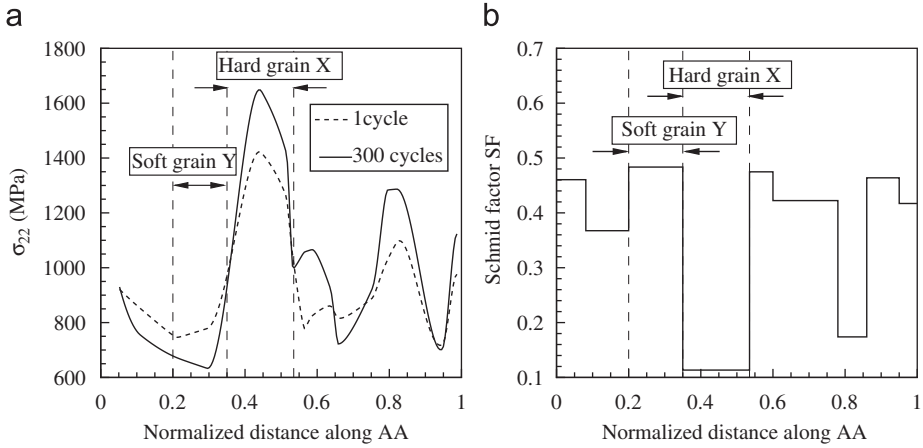


Fig. 4. Distribution of local variables from a simulation of the CPFE model of critical microstructure of specimen 1: (a) the loading direction stress (σ_{22}), and (b) the predominant prismatic Schmid factor along a section AA at the end of 1 and 300 dwell cycles.

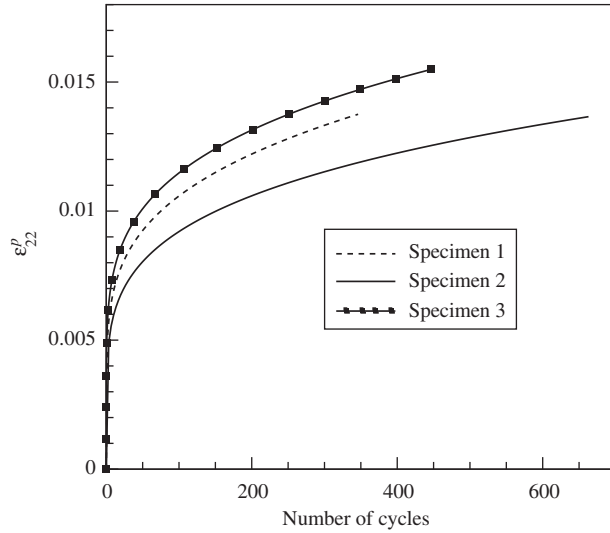


Fig. 5. Evolution of volume-averaged plastic strain with number of cycles for the three critical microstructures.

grain combination, as evidenced from the prismatic slip system Schmid factor (SF) plot in Fig. 4(b). A stress peak is seen in the grain X and a stress valley in the grain Y in Fig. 4(a). The stress peak at X after the 300 cycles is considerably higher than that after the first cycle. Also, this magnitude is much higher than the applied stress of 869 MPa. The peak stress increases with the number of cycles or time, while the valley keeps dropping with time. This is the consequence of load shedding from the grains adjacent to X, which undergo significant time-dependent plastic strain or creep. Fig. 4(b) shows that the hard oriented grain X has a much lower SF (~ 0.11) than its neighboring soft oriented grain Y, which has a high SF (~ 0.49). This large mismatch in SF is responsible for load shedding from the soft grain at Y onto the hard grain at X. Similar observations have also been made in Hasija et al. (2003), Deka et al. (2006), Venkatramani et al. (2006), and Venkataramani et al. (2007, 2008). This load shedding induced stress concentration in the hard grains provides a foundation for developing the grain-level crack nucleation in a polycrystalline Ti alloy microstructure. Volume-averaged plastic strains (ε_{22}^p) in the loading direction are plotted as functions of the number of cycles, for the critical microstructures of the three specimens, in Fig. 5. The microstructure of specimen 3 shows the maximum plastic strain, while that of specimen 2 shows the least.

3. Experimental crack observations in a cyclic dwell test

3.1. Crack nucleation site for dwell loading

Extensive experimental studies on the relation between crack evolution and crystallographic orientations in samples of Ti-6242 have been conducted in Sinha et al. (2006a) using quantitative tilt fractography and electron back scattered

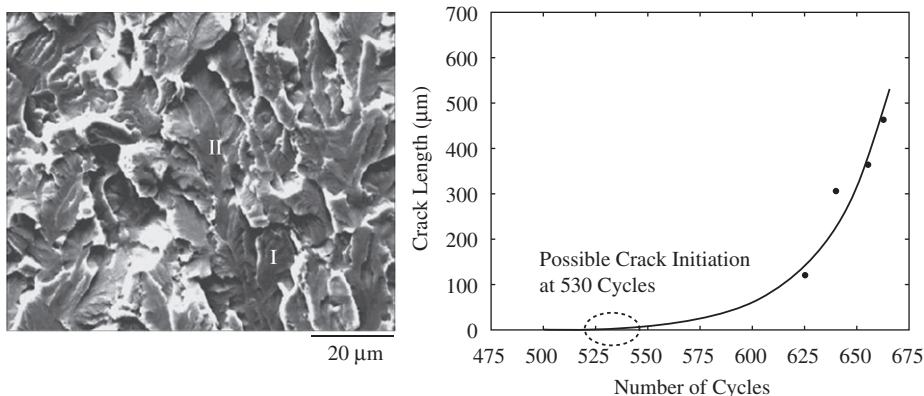


Fig. 6. (a) Fractograph of a faceted nucleation site for a failed Ti-6242 dwell fatigue specimen, (b) crack length as a function of number of cycles for a secondary crack in specimen 2.

Table 1

Primary crack nucleation data by ultrasonic monitoring in dwell fatigue experiments on Ti-6242.

Specimen #	Test type	Specimen life (cycles)	Cycles to crack nucleation	% life at primary crack nucleation
1	2-min dwell load	352	—	—
2	2-min dwell load (with modulation)	663	550	83
3	2-min dwell load (with modulation)	447	380	85

diffraction (EBSD) techniques in SEM. Fig. 6(a) shows the fractograph of a small region of crack nucleation site for a failed Ti-6242 specimen in dwell fatigue. Failure sites are found to be predominantly at those locations where the basal plane is nearly orthogonal to the principal loading direction (Sinha et al., 2006a; Bache, 2003). These sites consist of facets that form on the basal plane of the primary α grains. In Sinha et al. (2006b), the angle θ_c between the loading axis and the crystallographic *c*-axis at the failure site has been found to be quite small ($\sim 0\text{--}30^\circ$). Furthermore, the failure site shows a low prism activity with the Schmid factor $SF \sim 0\text{--}0.1$ and a moderate basal activity with $SF \sim 0.3\text{--}0.45$. However, the region surrounding the failure site has a high prismatic and basal activity with $SF \sim 0.5$. The overall inference from these observations is that while crack nucleation occurs in a region that is unfavorably oriented for slip (hard grain), it is surrounded by grains that are favorably oriented for slip (soft grain). These observations also suggest that time-dependent accumulation of stress in the hard oriented grains due to load shedding with increasing plastic deformation in the surrounding soft grains. This is responsible for crack nucleation in Ti alloys under creep and dwell loading.

3.2. Detection and monitoring cracks in mechanical tests

Ultrasonic techniques, such as *in situ* surface acoustic wave techniques, have been developed for monitoring subsurface crack nucleation in high micro-texture α/β forged Ti-6242 specimens for dwell fatigue and creep experiments in Rokhlin et al. (2005). The experiments monitor crack nucleation and growth in real time, making estimation of the time for crack nucleation possible. Dwell fatigue experiments are conducted with the three microstructural specimens mentioned in Section 2.2. The specimens 1, 2 and 3 fail after 352, 663 and 447 cycles, respectively. In Rokhlin et al. (2005) and Williams (2006) crack growth in specimens 2 and 3 is monitored through micro-radiographic images taken by interrupting the experiment every 15 cycles. Fig. 6(b) is a representative plot of the observed crack length as a function of the number of cycles for a secondary crack in specimen 2. This crack is of length 125 μm at 625 cycles, while at 663 cycles, it is of length 470 μm. In Fig. 6(b), the plot is extrapolated backwards to zero length to estimate the number of cycles to crack nucleation. For this specimen, crack nucleation is estimated to be approximately at 530 cycles. The number of cycles to crack nucleation, obtained by extrapolating plots for primary cracks that grew to cause final failure, are given in Table 1. The primary crack initiated at 83% life (550 cycles) for specimen 2, while it nucleated at 85% life (380 cycles) for specimen 3. The results generally suggest that primary crack nucleation in dwell fatigue occurs in the range 80–90% of the total number of cycles to failure.

4. Review and evaluation of some microstructure-based failure models

A few existing microstructure-based failure models are examined for dwell fatigue crack nucleation in polycrystalline Ti alloys in this section. Results of the CPFE simulations in Section 2.2 are used as inputs to these models. The failure predictions by these models are compared with the experimental observations of Section 3.

4.1. Dislocation-based Stroh-type crack nucleation models

Stress concentration induced mode-I crack nucleation at the grain boundary of a crystalline solid has been modeled in Stroh (1954) using a dislocation pileup model. The model proposes that a crack is nucleated under the condition that

$$n\sigma_0 \geq 12\alpha G \quad (8)$$

where n is the number of dislocations in the pileup, σ_0 is the applied stress on the slip plane, G is the shear modulus and $\alpha = \gamma_s/bG$ is a material constant in terms of γ_s , the surface energy and b the Burgers vector.

Crack nucleation by dislocation pileups has also been studied in Smith (1979, 1966), where it was proposed that a dislocation pileup leads to a mode-II crack by dislocation coalescence. Dislocation pileup is represented from equilibrium consideration in a grain of size d , yielding a cleavage fracture criterion as

$$\sigma_E \geq \left(\frac{2\gamma_s G}{\pi(1-\nu)d} \right)^{0.5} \quad (9)$$

In this model, the stress σ_E required to fracture a grain is inversely related to the square root of the grain size. While the functional forms are different, both models assume that the crack nucleates at the hard–soft grain boundary as a consequence of stress concentration caused by dislocation pileup in the soft grain.

However, these early local models of metal fracture have some serious limitations with respect to failure prediction in Ti alloys. They lack the combined effect of multi-axial (normal and shear) stresses on crack nucleation. Furthermore, only one slip system in one slip plane is considered, and the interaction of different slip systems are not accounted for.

4.2. A purely stress-based nucleation criterion

A purely stress-based criterion has been tested in Kirane and Ghosh (2008). In this model, a crack is nucleated when an effective mixed-mode stress exceeds a critical value, i.e. $T_{eff} \geq T_{crit}$. Results of CPFE simulations show that the rate of change of T_{eff} per cycle is very low at higher cycles, with saturation in hardness (increases only by 3.7% in the last 250 cycles). For a constant T_{crit} , even a small variation in T_{crit} will cause the predicted life to change by hundreds of cycles. For example, a 3.5% change in T_{crit} from 1660 to 1724 MPa results in a 150% change in the predicted life from 100 cycles to 352 cycles. This is not an observed phenomenon and requires an amendment with the incorporation of other evolving variables.

4.3. Energy-based approaches for micro-crack nucleation

An approach for predicting micro-crack nucleation, based on the Gibbs free energy change due to the nucleation of a micro-crack from a metastable assembly of defect structures during cyclic deformation, has been proposed in Lin et al. (1986) and Yao et al. (2007). An energy barrier must be overcome during the formation of a fatigue crack due to the energy required to create new surfaces. A fatigue crack spontaneously nucleates when the energy accumulated in slip bands reaches a critical value, given by a maximum in the plot of Gibbs free energy change versus the number of cycles. Prior to nucleation, the accumulated damage is in the form of increased lattice defects. The area of the stress–plastic strain hysteresis loop is a measure of the total mechanical energy spent during the cycling loading process. Most of the irreversible energy is converted to heat and only a small portion of this irreversible energy is stored as defects, which is taken care of through an efficiency parameter f in this model.

A particular form of this class of models, developed in Bhat and Fine (2001), is tested for Ti alloys. By assuming the nucleation of a penny-shaped crack of length a^* , the fatigue damage accumulated in each cycle is derived in Bhat and Fine (2001) as

$$f_d = \int_N \frac{\pi E f t \Delta\sigma \Delta\varepsilon_p}{\pi E \gamma_s - 4\sigma^2 a^*(1-\nu^2)} dN \quad (10)$$

where E is Young's modulus of elasticity, ν is Poisson's ratio, t is the thickness of the region around the micro-crack that is drained of defects when the crack forms, σ is maximum stress in the cycle, $\Delta\sigma$ and $\Delta\varepsilon_p$ are stress and plastic strain ranges in the cycle, and γ_s is the surface energy per unit area for formation of new crack surfaces.

In examining this model for Ti alloys, γ_s is taken as 5 N/m, $E=128$ GPa and $\nu=0.33$. Eq. (10) is integrated over the cycles to calculate the cumulative fatigue damage parameter d_f at each Gauss point in the finite element mesh. For the material in consideration, the critical size of penny-shaped micro-crack a^* is assumed to be 50 nm. The size of the region is assumed to be $t=40$ nm, which is of the same order as the size of nucleation zone in Yao et al. (2007). The efficiency parameter f is calibrated from the experimental data for number of cycles for nucleation of micro-crack in Ti-6242. The number of cycles for the three microstructural specimens are given in Tables 1 and 2. Crack nucleation in the specimen 1 is assumed at 85% of the total life, viz. 300 cycles. The cumulative fatigue damage d_f evolution with number of cycles for this microstructure is shown in Fig. 7(a). Micro-crack nucleation occurs when the parameter d_f reaches 1. From this figure, the efficiency parameter f is calibrated as 0.0125. The other specimens 2 and 3 are similarly analyzed using $f=0.0125$ and the evolution of cumulative fatigue damage d_f with cycles are plotted in Fig. 7(b). The predicted number of cycles for micro-crack nucleation are 127 and 167 for critical microstructures of specimens 2 and 3 respectively. However, the corresponding

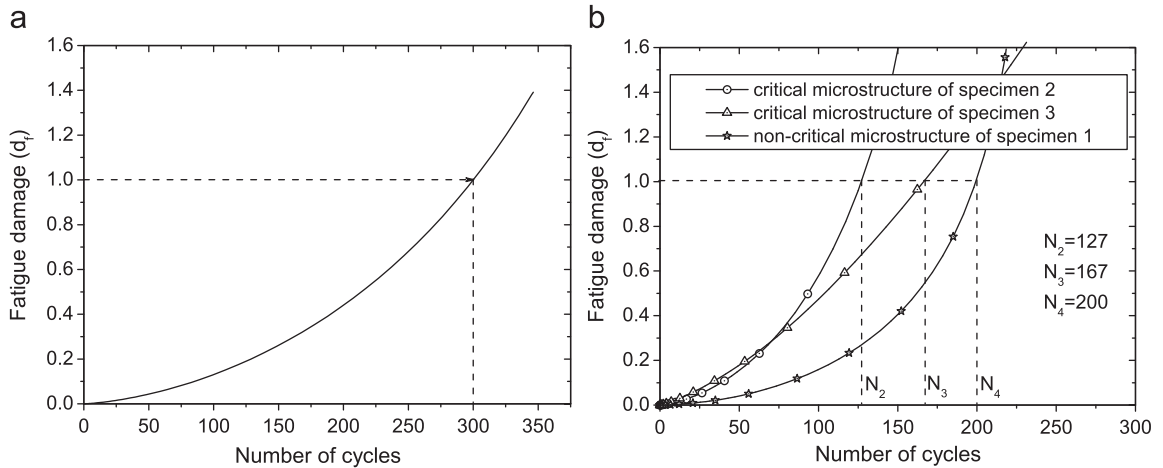


Fig. 7. Evolution of fatigue damage with cycles: (a) calibration of the efficiency parameter f from critical microstructure of specimen 1, (b) prediction of number of cycles to micro-crack nucleation for three different microstructures.

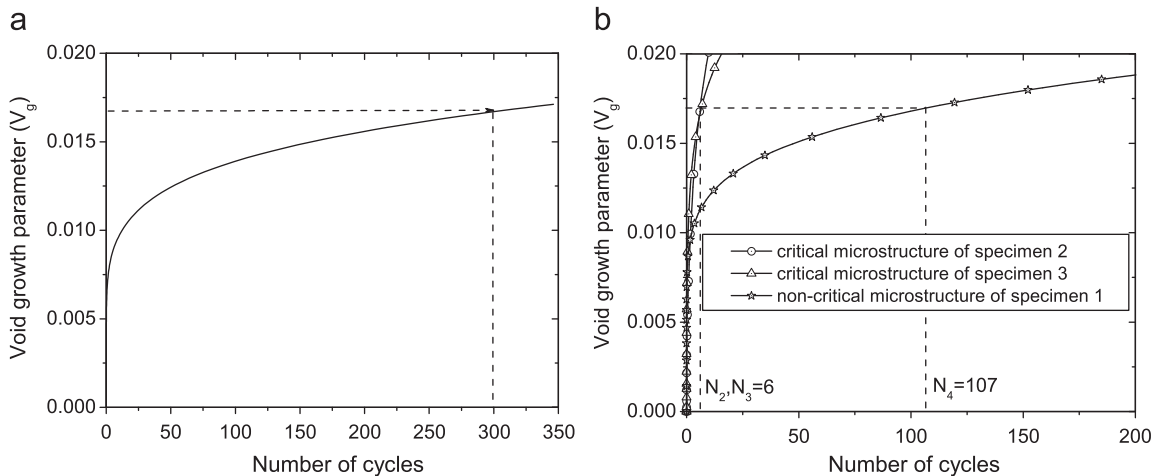


Fig. 8. Evolution of a void growth parameter V_g with cycle: (a) calibration of critical V_g for micro-crack nucleation in the critical microstructure of specimen 1, (b) prediction of the number of cycles for micro-crack nucleation for three other microstructures.

experimental values are 530 and 380 respectively. Also, for a non-critical microstructure of specimen 1, where no crack was experimentally observed, this model predicts crack nucleation at 200 cycles. This energy-based approach is thus not suitable for predicting fatigue crack nucleation in these Ti alloys.

4.4. Micro-void growth models for prediction of micro-crack nucleation

Some micro-crack nucleation criteria in the literature have used micro-void growth models, e.g. in Rice and Tracey (1969), which consider the effect of stress multi-axiality and plastic strain evolution. A void-growth parameter V_g is expressed in these models as

$$V_g = \int_{\varepsilon_{eq}^p} c_1 \exp \frac{3}{2} \frac{\sigma_m}{\sigma_{eq}} d\varepsilon_{eq}^p \quad (11)$$

where σ_m is the hydrostatic stress, σ_{eq} is the von Mises stress and ε_{eq}^p is the equivalent plastic strain. The constant c_1 has been given as 0.283 in Rice and Tracey (1969). For using this model in predicting crack nucleation, a critical value of V_g is calibrated from CPFE simulations of the critical microstructure of specimen 1. The evolution of V_g is shown in Fig. 8(a) for this microstructure. Knowing the experimental value of the number of cycles to micro-crack nucleation as ~ 300 , the critical void growth parameter is calibrated from Fig. 8(a) as 0.016755. This value is subsequently used to predict the number of cycles for micro-crack nucleation in the critical microstructures of specimens 2 and 3 as well as in the

Table 2

Comparison of predicted cycles to crack nucleation with experimentally observed life.

Microstructure label	Cycles to crack nucleation (experiment)	Cycles to crack nucleation (predicted)		% relative error	
		80% of life	85% of life	80% of life	85% of life
Specimen 2	530	534	567	+0.72	+6.93
Specimen 3	380	385	405	+1.35	+6.49

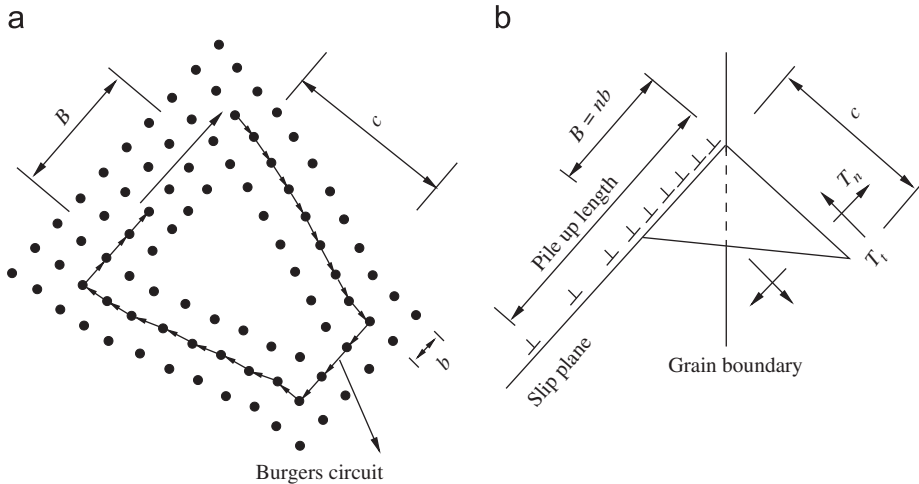


Fig. 9. (a) A wedge crack with opening displacement of $4b$, produced by coalescence of four dislocations, (b) nucleation of a wedge crack in the hard grain resulting from a dislocation pileup in the soft grain.

non-critical microstructure of specimen 1. Fig. 8(b) shows the evolution of V_g . The number of cycles for micro-crack nucleation are predicted as 6, 6 and 107 for the critical microstructures of specimens 2 and 3 and the non-critical microstructure of specimen 1 respectively. This predicted cycles to failure do not match with experimental data in Table 2. Again, these type of models are not suitable for accurate life prediction for titanium alloys considered in this work.

5. A new non-local crack nucleation criterion from CPFE variables

5.1. Model description

The inter-granular crack nucleation model is built on the premise that a wedge crack nucleates in the neighboring grain as a dislocation approaches the grain boundary. An edge dislocation, which is an extra half-plane of atoms wedged between two complete planes, is equivalent to a micro-crack with opening displacement of one atomic spacing b . As more dislocations are piled up, the opening displacement increases in size as shown in Fig. 9(a). The crack opening displacement corresponds to the closure failure along a circuit, surrounding the piled-up dislocations. If n edge dislocations of Burger's vector b contribute to the formation of a micro-crack, a wedge with opening displacement $B = nb$ is produced. It should be noted that while the dislocations are piled up at the grain boundary of a soft grain, the wedge crack initiates in the adjacent hard grain as shown in Fig. 9(b).

The micro-crack length c in Fig. 9(a) can be considered as the length after which the disturbance in the lattice structure of the hard grain subsides. This disturbance is caused by extra half-planes of atoms in the soft grain. This micro-crack length c may be related to crack opening displacement B using two different formulae as:

- (i) With a 90° intercept definition suggested in Rice (1968),

$$c_1 = B/2 \quad (12)$$

This formula is commonly used to infer crack opening displacements in FE analyses of cracks Anderson (2005).

- (ii) The equilibrium length of a wedge crack with an opening displacement B is related to the elastic properties and surface energy in Stroh (1954) as

$$c_2 = \frac{G}{8\pi(1-\nu)\gamma_s} B^2 \quad (13)$$

where ν is Poisson's ratio and G is the shear modulus.

The suitability of c_1 or c_2 as crack length in the crack nucleation criterion is decided based on their relative accuracy, when compared with experiments in Section 6.

The wedge crack is initially stable. As more dislocations enter the crack, the crack opening size increases, causing the crack length to grow. Additionally, the stress in the hard grain across the micro-crack also aids in the opening up of the crack. The multi-axial stress acting on the micro-crack surface is a combination of normal and shear stresses as shown in Fig. 9(b). It is assumed that cracks nucleate (grow) from the tip, when the mixed-mode stress intensity factor K_{mix} exceeds a critical value, K_c . K_{mix} is expressed in terms of normal stress intensity factor, K_n and shear stress intensity factor K_t as

$$K_{mix}^2 = K_n^2 + \beta K_t^2 \quad (14)$$

where β is a shear stress factor, which is used to assign different weights to the normal and shear traction components for mixed mode. In Ruiz et al. (2001), β is defined as the ratio of the shear to normal fracture toughness of the material, i.e. $\beta \approx K_{nc}/K_{tc}$. A value of $\beta = 0.7071$ is suggested for Ti-64 alloys in Parvatareddy and Dillard (1999), and is used in this study. Using the definitions for stress intensity factors $K_n = \langle T_n \rangle \sqrt{\pi c}$ and $K_t = T_t \sqrt{\pi c}$ and noting that the micro-crack grows when $K_{mix} \geq K_c$, the hard grain crack nucleation criterion, ahead of dislocation pile ups in adjacent soft grain is stated as

$$T_{eff} = \sqrt{\langle T_n \rangle^2 + \beta T_t^2} \geq \frac{K_c}{\sqrt{\pi c}} \quad (15)$$

or equivalently

$$R = T_{eff} \cdot \sqrt{c} \geq R_c \quad \text{where } R_c = \frac{K_c}{\sqrt{\pi c}} \quad (16)$$

T_{eff} is an effective stress for mixed-mode crack nucleation. It is expressed in terms of the stress component normal to the crack surface $T_n = \sigma_{ij} n_i^b n_j^b$ and the tangential stress component $T_t = \|\mathbf{T} - T_n \mathbf{n}^b\|$. Here \mathbf{T} is the stress vector on the crack surface, σ_{ij} is the Cauchy stress tensor and n_i^b are the components of unit outward normal to the crack surface. Only the tensile normal stress $\langle T_n \rangle$, represented by the McCauley bracket $\langle \rangle$, contributes to the effective stress responsible for crack opening. Sensitivity analysis with different values of β indicate that T_{eff} is not very sensitive to β for $\langle c+a \rangle$ oriented hard grains, since $T_n \gg T_t$. It is worth noting that the stress components in (15) are remote applied stresses. However, since the typical values of c that cause unstable cracking are of the order of nanometers, while the typical grain size is of the order of microns, it is reasonable to consider the maximum stress at the hard grain boundary as the remote stress. As more dislocations are added to the pileup with time, the wedge crack opening displacement and length increase. This implies that a smaller T_{eff} is needed to initiate a crack with increasing plastic deformation and pileup. This contributes to the non-locality aspect of the crack nucleation criterion.

The parameter R_c in Eq. (16) depends on the elastic properties as well as on the critical strain energy release rate G_c . It has the units of stress intensity factor ($\text{MPa} \sqrt{\mu\text{m}}$). It is calibrated from crack nucleation data extracted from a combination of experiments and simulations on a single microstructure.

5.2. Numerical implementation of the crack nucleation criterion

This section describes a method for calculating micro-crack opening displacement B , required in Eq. (12) or (13) to estimate the micro-crack length. Crack nucleation is examined on different planes in the hard grain of the polycrystalline microstructure.

For estimating B , it is necessary to know the distribution of dislocations inside the soft grain. The crystal plasticity model discussed in Section 2 does not explicitly have dislocation density as a state variable. Hence the plastic strains and their gradients that are available from the results of the CPFE simulations are used to estimate the micro-crack opening displacement B . The wedge opening displacement in Fig. 9(a) is equal to the closure failure along a circuit surrounding the piled-up edge dislocations on one slip plane. This can be extended to a generalized 3D representation of dislocations for multiple slip systems. The corresponding closure failure, which is manifested as the crack opening displacement, is a vector quantity. In the dislocation glide model, the lattice incompatibility can be measured by the closure failure of a line integral along a Burgers circuit $\bar{\Gamma}$ in the intermediate configuration. Closure failure is equivalent to the net Burgers vector \mathbf{B} of all dislocations passing through the region $\bar{\Omega}$, bounded by the circuit. The Burgers vector can be mapped to a line integral along a referential circuit, Γ using the plastic deformation gradient \mathbf{F}^p . Using Stoke's theorem, the closure failure is related to the surface integral of the curl of \mathbf{F}^p over a referential surface Ω as

$$\mathbf{B} = \oint_{\bar{\Gamma}} d\bar{\mathbf{x}} = \oint_{\Gamma} \mathbf{F}^p \cdot d\mathbf{X} = \int_{\Omega} \mathcal{A} \cdot \mathbf{n} \, d\Omega \quad (17)$$

where \mathbf{n} is the unit normal to the surface Ω and \mathcal{A} is Nye's dislocation tensor given in Eq. (7). Components of \mathcal{A} are evaluated at each quadrature point using shape function-based interpolation of nodal values of \mathbf{F}^p , as described in Anahid et al. (2009).

The closure failure obtained from Eq. (17) can make any arbitrary angle with respect to the surface, depending on the type of dislocations passing through $\bar{\Omega}$. It also depends on the angle between dislocation line and the surface. For pure edge dislocation with the dislocation line perpendicular to $\bar{\Omega}$, the closure failure \mathbf{B} lies in the plane, as shown in Fig. 10(a). If the dislocation line is not perpendicular to $\bar{\Omega}$, the closure failure does not lie in the plane. For pure screw dislocation with

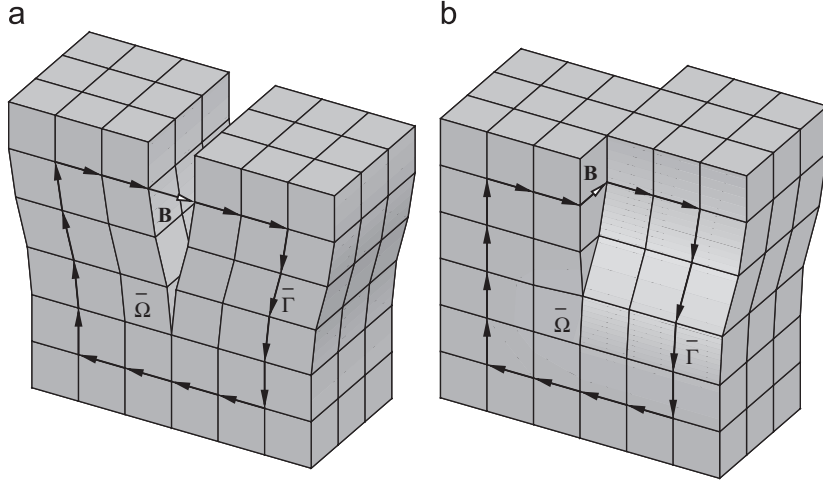


Fig. 10. Closure failure and crack opening displacement for (a) single pure edge dislocation, and (b) single pure screw dislocation.

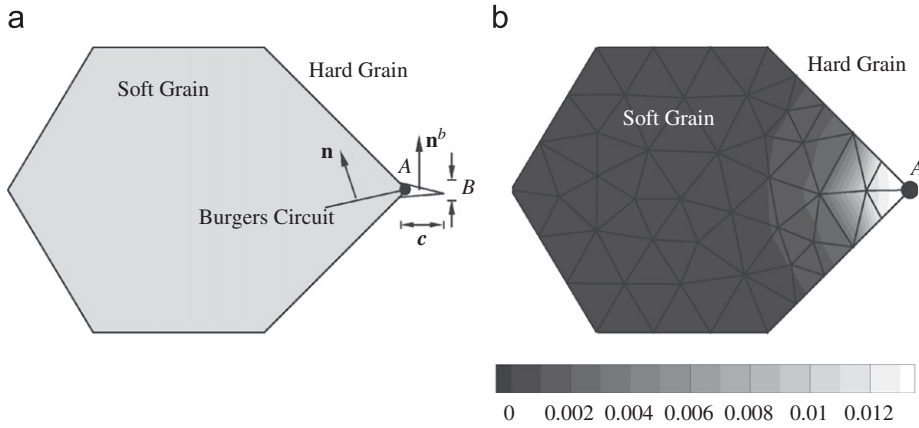


Fig. 11. (a) Wedge-crack in the hard grain as a result of dislocation pileup in adjacent soft grain, (b) distribution of the norm of Nye's dislocation tensor inside a representative soft grain.

a dislocation line perpendicular to $\bar{\Omega}$, \mathbf{B} is also perpendicular to the plane, as shown in Fig. 10(b). For a mixed type of dislocation with edge and screw components, \mathbf{B} is neither perpendicular nor parallel to Ω .

Consider a point A on the hard–soft grain boundary, shown in Fig. 11(a), which impedes dislocations generated from a source in the soft grain. There are different planes with different normal vectors which contain point A . The closure failure caused by dislocations piercing each of these planes depends on the normal, \mathbf{n} , based on Eq. (17). The stresses on each of the resulting micro-cracks are also different. Consequently, there are different possible competing micro-cracks with dissimilar stress intensity factors at point A . The crack with the highest mixed-mode stress intensity factor is considered as the critical one. If the unit normal to the unit area surrounded by a Burgers circuit containing point A in Fig. 11(a) is denoted by \mathbf{n} , the size of crack opening displacement B is calculated using Eq. (17) as

$$B = \|\mathcal{A} \cdot \mathbf{n}\| \quad (18)$$

This is used in either Eq. (12) or (13) to estimate the crack length c . Neglecting the effect of screw dislocations on the wedge crack opening, the unit normal to the wedge crack surface is obtained as

$$\mathbf{n}^b = \frac{\mathcal{A} \cdot \mathbf{n}}{B} \quad (19)$$

The effective stress T_{eff} on the wedge crack surface is measured using the procedure described in Section 5.1. The mixed-mode stress intensity factor that corresponds to the wedge crack produced by dislocations passing through the unit area surface with unit normal of \mathbf{n} is obtained as

$$K_{mix} = T_{eff} \sqrt{\pi c} \quad (20)$$

This procedure is executed for all possible \mathbf{n} vectors in 3D space. The vector \mathbf{n}_{cr} , which yields the highest stress intensity factor, is considered as the critical normal vector. The critical crack opening displacement at the hard–soft grain boundary is then obtained as $\mathbf{B}_{cr} = A \cdot \mathbf{n}_{cr}$. This relation is true when all dislocations are concentrated in a very small portion of the soft grain, surrounding the point A . However, dislocations are distributed in the entire soft grain. Fig. 11(b) shows the contour of the norm of Nye's dislocation tensor inside a representative soft grain. The maximum value occurs at the hard–soft grain boundary (point A), and the values decrease with increasing distances from the grain boundary. A is available at the Gauss point of all the tetrahedron elements within the soft grain from the CPFE simulations. Each element I contains its own dislocations quantified by Nye's dislocation tensor A_I at that element. Dislocations associated with element I produce a crack opening displacement as

$$\mathbf{B}_I = W_I A_I A_I \cdot \mathbf{n}_{cr} \quad (21)$$

Here A_I is the surface area associated with element I , into which the dislocations penetrate. It is estimated through the assumption of an equivalent spherical domain that has the same volume as the element. The center of this sphere is assumed to coincide with the element integration point. Assuming that the plane containing the Burgers circuit in the element I passes through the integration point, A_I is equal to the circular cross-sectional area passing through the center of sphere, expressed as

$$A_I = \pi R_I^2 = 1.77(V_I)^{2/3} \quad \text{where } R_I = \sqrt[3]{\frac{3}{4\pi}V_I} \quad (22)$$

V_I is the element volume and R_I is the sphere's radius. A weighting parameter W_I is introduced to \mathbf{B}_I to account for the diminishing effect of a dislocation on the crack opening displacement with distance. A formula $W_I = \exp(-r_I^2/2l^2)$, where r_I is the distance from the point with maximum dislocation density (A in Fig. 11(b)) has been proposed in Engelen et al. (2003). This expression is used for the I -th element integration point. $W_I \rightarrow 0$ beyond a critical distance l and $W_I=1$ when $r_I=0$. Thus the crack opening displacement B , accounting for the contribution of all elements in the soft grain on the hard grain crack, is stated as

$$B = \|\mathbf{B}\| = \left\| \sum_I \mathbf{B}_I \right\| = \left\| \sum_I W_I A_I A_I \cdot \mathbf{n}_{cr} \right\| \quad (23)$$

Defining an effective dislocation tensor as

$$\mathbf{D}_{eff} = \sum_I W_I A_I A_I \quad (24)$$

Eq. (23) can be rewritten as

$$B = \|\mathbf{D}_{eff} \cdot \mathbf{n}_{cr}\| \quad (25)$$

Using the 90° intercept, defined in Section 5.1, to estimate the micro-crack length, c is obtained using Eqs. (25) and (12) as

$$c_1 = \frac{1}{2} \|\mathbf{D}_{eff} \cdot \mathbf{n}_{cr}\| \quad (26)$$

If Eq. (13) is used to relate the micro-crack length to the crack opening displacement, c is estimated as

$$c_2 = \frac{G}{8\pi(1-\nu)\gamma_s} \|\mathbf{D}_{eff} \cdot \mathbf{n}_{cr}\|^2 \quad (27)$$

With material properties set to $G=48$ GPa, $\nu=\frac{1}{3}$ and $\gamma_s=5$ N/m, this equation is written as

$$c_2 = 573 \times 10^6 \|\mathbf{D}_{eff} \cdot \mathbf{n}_{cr}\|^2 \quad (\text{in m}) \quad (28)$$

The unit normal to the wedge crack surface in the hard grain is

$$\mathbf{n}^b = \frac{\mathbf{D}_{eff} \cdot \mathbf{n}_{cr}}{\|\mathbf{D}_{eff} \cdot \mathbf{n}_{cr}\|} \quad (29)$$

The effective traction T_{eff} is updated using the procedure described in Section 5.1 and \mathbf{n}^b from Eq. (29). Finally, T_{eff} and c are used in Eq. (16) to calculate the effective nucleation variable R . R is checked for every grain pair in the CPFE model at the post-processing stage. The condition posed in Eq. (16) is non-local, since the stress required to initiate a crack at a point in the hard grain depends on the gradient of plastic strain in the neighboring soft grains.

5.3. The Cottrell–Petch fracture model as a limiting case of the nucleation model

A schematic diagram explaining the Cottrell–Petch fracture model (Cottrell, 1958; Petch, 1959) is shown in Fig. 12. It shows a pileup of n positive edge dislocations on a single slip plane, impeded by the grain boundary. If it is assumed that all the dislocations coalesce and form a wedge type micro-crack normal to the applied tensile stress σ_f , the fracture stress

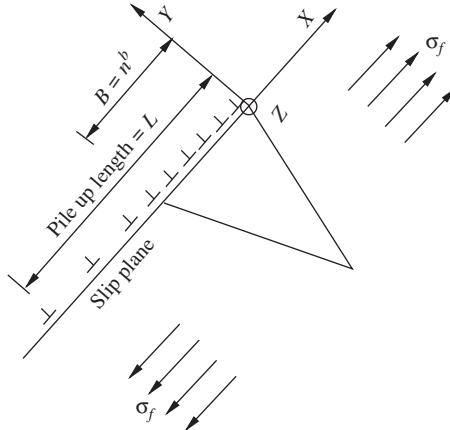


Fig. 12. A schematic diagram explaining of Cottrell–Petch fracture model.

is given as (Cottrell, 1958; Petch, 1959)

$$\sigma_f = \frac{2\gamma_s}{nb} \quad (30)$$

The proposed crack nucleation model is shown to reduce to the Cottrell–Petch model in the limiting case of one active slip system in which only edge dislocations slip on a single plane.

To derive this limiting case, the origin of the Cartesian coordinate system is fixed on the leading dislocation with X- and Y-axes oriented along the slip direction and slip plane normal respectively, as shown in Fig. 12. The Z-axis points out of page. For a single active slip system, the plastic slip rate $\dot{\gamma}^x$ on slip systems other than the active one is zero. Slip direction and normal vectors \mathbf{m}_0 and \mathbf{n}_0 are equal to the unit vectors along X and Y directions respectively. Eq. (3) can be rewritten in terms of the plastic slip on the active system γ as

$$\mathbf{L}^p = \dot{\mathbf{F}}^p \mathbf{F}^{p-1} = \dot{\gamma} \mathbf{m}_0 \otimes \mathbf{n}_0 \quad (31)$$

The only non-zero component of the plastic velocity gradient tensor is $\mathbf{L}_{12}^p = \dot{\gamma}$. The corresponding plastic deformation gradient and Nye's dislocation tensor in matrix form are

$$\mathbf{F}^p = \begin{bmatrix} 1 & \gamma & 0 \\ 0 & 1 & 0 \\ 0 & 0 & 1 \end{bmatrix}, \quad \Lambda = \begin{bmatrix} -\frac{\partial \gamma}{\partial Z} & 0 & \frac{\partial \gamma}{\partial X} \\ 0 & 0 & 0 \\ 0 & 0 & 0 \end{bmatrix} \quad (32)$$

Nye's dislocation tensor is zero for any point outside the slip plane. For any point on the slip plane it can be obtained from Eq. (32). Substituting Λ in Eq. (32) and in Eq. (17), the closure failure is obtained to be always along the slip direction (X-axis) for any arbitrary \mathbf{n} vector. The closure failure caused by dislocations passing through a unit area on the plane normal to X-axis is equal to $-\partial \gamma / \partial Z$. These dislocations are of screw type, parallel to the slip direction. If no screw dislocation is present, $-\partial \gamma / \partial Z = 0$. Therefore Nye's dislocation tensor can be reduced to

$$\Lambda = \begin{bmatrix} 0 & 0 & \frac{\partial \gamma}{\partial X} \\ 0 & 0 & 0 \\ 0 & 0 & 0 \end{bmatrix} \quad (33)$$

Following the procedure outlined in Section 5.2, \mathbf{n}_{cr} is obtained as the unit vector along the Z direction. In the Cottrell–Petch model, all dislocations in the pileup have the same contribution to the crack opening displacement, and hence the weighting parameter in Eq. (24) is 1 for all dislocations. Eq. (24) may be written in a continuous form as

$$\mathbf{D}_{eff} = \int_{\Omega} \Lambda d\Omega \quad (34)$$

where Ω is an area surrounding the dislocation pileup. If ρ is the dislocation density per unit length, it can be shown that $(\partial \gamma / \partial X) d\Omega = \rho b dX$ at any point A on the dislocation pileup, where $d\Omega$ is an infinitesimal area around point A. Thus,

$$\int_{\Omega} \frac{\partial \gamma}{\partial X} d\Omega = \int_0^L \rho b dX = nb \quad (35)$$

L and n denote the dislocation pileup length and number of dislocations in the pileup respectively. Using Eqs. (33)–(35) the effective dislocation tensor \mathbf{D}_{eff} is obtained as

$$\mathbf{D}_{\text{eff}} = \begin{bmatrix} 0 & 0 & nb \\ 0 & 0 & 0 \\ 0 & 0 & 0 \end{bmatrix} \quad (36)$$

This expression is used in Eq. (27) to calculate the wedge crack length c as

$$c = \frac{Gn^2 b^2}{8\pi(1-\nu)\gamma_s} \quad (37)$$

In the Cottrell–Petch model, the traction on the wedge crack has the normal component only, and hence $T_{\text{eff}}=T_n$ in Eq. (15). Also the mixed-mode fracture toughness, K_c , should be replaced by the normal fracture toughness K_{nc} , which equals to

$$K_c = K_{nc} = \sqrt{\frac{4G\gamma_s}{1-\nu}} \quad (38)$$

Using Eqs. (16), (37) and (38), the crack nucleation criterion is simplified to

$$T_n nb \geq 4\sqrt{2}\gamma_s \quad (39)$$

In other words, the local fracture stress based on the proposed crack nucleation model is

$$T_n = \frac{4\sqrt{2}\gamma_s}{nb} \quad (40)$$

From this equation, the tensile stress required for crack nucleation is deduced to be $2\sqrt{2}$ times the fracture stress proposed by Cottrell–Petch model in Eq. (30). The reason for this difference is that the stress in Eq. (40) is the local stress, while Eq. (30) is based on the applied stress. The CPFE simulations in Section 6 shows that the local effective stress T_{eff} at failure site is generally $\sim 2\text{--}3$ times larger than the applied stress, which is consistent with the difference between Eqs. (30) and (40).

6. Parameter calibration and validation of the crack nucleation criterion

Experimental data from Section 3.2 are used again for calibrating and validating the proposed crack nucleation model in Section 5. The number of cycles to major crack nucleation under dwell loading for the three microstructural specimens are given in [Tables 1 and 2](#). Based on the observations made in the experiments, crack nucleation in the critical microstructure of specimen 1 is assumed at two different percentages of the total life, viz. 80% and 85%. This corresponds to 282 and 300 cycles respectively. This data is used for calibrating the parameter R_c in Eq. (16). As a validation exercise, the calibrated value of R_c is used to predict the number of cycles to crack nucleation in specimens 2 and 3. It is expected that the nucleation criterion will be met at some locations in the CPFE models of the critical microstructures, but will not be satisfied for the non-critical microstructure.

6.1. Calibration of R_c for α/β forged Ti-6242

The crack nucleation parameter R_c in Eq. (16) is calibrated from results of 2-min dwell fatigue CPFE simulations of a critical microstructure of specimen 1. Crack nucleation is assumed at 282 and 300 cycles, corresponding to 80% and 85% of the total life of ~ 352 cycles respectively. The variable R in the LHS of Eq. (16) is determined for all grain pairs at the end of 282 and 300 cycles respectively, as follows:

- For each grain pair in the microstructure, a constituent grain is designated as hard or soft based on the amount of plasticity and stress concentration.
- For each grain in the pair, elements with a common triangular edge on the shared boundary are determined. The nodes of these triangles are the common nodes between the two grains.
- For each common node on the shared boundary, the procedure in Section 5.2 is implemented to obtain the critical normal vector \mathbf{n}_{cr} and the stress intensity factor associated with this normal vector. Nye's dislocation tensor at each common node, which is required to estimate c , is obtained from the integration points in the surrounding elements inside the soft grain. A weighted averaging scheme, described in [Anahid et al. \(2009\)](#), is used for this purpose. Correspondingly, the nodal values of stress components are calculated from the integration points in the surrounding elements inside the hard grain.
- The common node with the highest stress intensity factor is chosen. This corresponds to the point A in Section 5.2. Consequently, the variable R is obtained for the grain pair using Eqs. (22)–(29).

It should be noted that the R value depends on the equation used to estimate micro-crack length c . If Eq. (26) is used to calculate c , the resulting R value is denoted by R_1 . Otherwise, if Eq. (28) is used to determine c , the R value is denoted by R_2 . The hard grain with the maximum value of R_1 is identified and the evolution of this maximum R_1 with the number of

cycles is plotted in Fig. 13(a). Two limiting values of R_c are determined from the values of R_1 at 282 and 300 cycles respectively. They are:

- $R_{c1(80\%)} = 60.84 \text{ MPa } \mu\text{m}^{1/2}$.
- $R_{c1(85\%)} = 61.45 \text{ MPa } \mu\text{m}^{1/2}$.

Histograms of R_1 at 282 and 300 cycles respectively are shown in Fig. 14(a) along a X-directed line passing through the hard–soft grain combination with the highest R_1 value. This line intersects 14 grain boundaries. Also the evolution of maximum R_2 with number of cycles is plotted in Fig. 13(b), and the critical R_c values are obtained from the values of R_2 at 282 and 300 cycles as:

- $R_{c2(80\%)} = 178.73 \text{ MPa } \mu\text{m}^{1/2}$.
- $R_{c2(85\%)} = 180.55 \text{ MPa } \mu\text{m}^{1/2}$.

Fig. 14(b) shows the histograms of R_2 at 282 and 300 cycles respectively along a X-directed line passing through the hard–soft grain combination with the highest R_2 value. This line intersects 15 grain boundaries. The calibrated values of R_c are subsequently used for predicting crack nucleation in other specimens.

Results of the CPFE simulation for the non-critical microstructure of specimen 1, described in Section 2.2, are post-processed to evaluate the values of R_1 and R_2 for all grain-pairs. Fig. 15(a) and (b) plots the evolution of maximum R_1 and maximum R_2 as a function of cycles respectively. The maximum R_1 reached at the end of 352 cycles is $44 \text{ MPa } \mu\text{m}^{1/2}$. This is less than both critical values $R_{c1(80\%)}$ and $R_{c1(85\%)}$ for both limiting cases. Also the maximum R_2 reached at the end of 352 cycles is only $95 \text{ MPa } \mu\text{m}^{1/2}$. This is also far less than the limiting values of R_{c2} . Thus the criterion predicts no crack

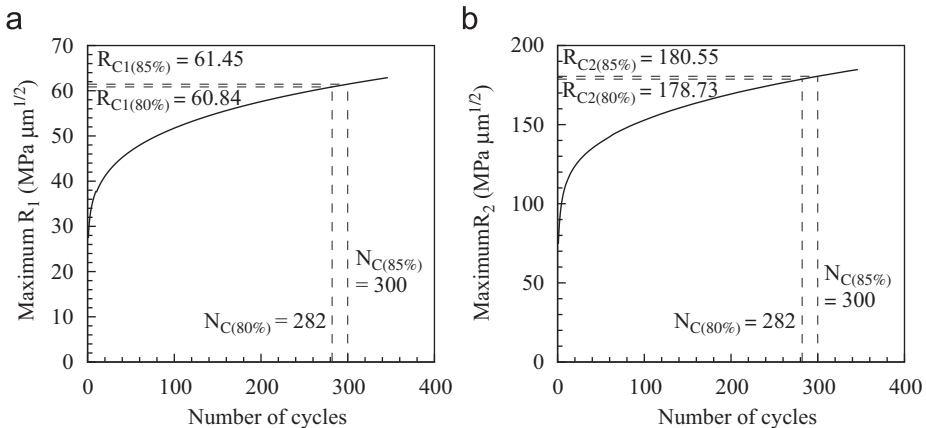


Fig. 13. (a) Evolution of the maximum R_1 over number of cycles for the FE model of critical microstructure of specimen 1, (b) evolution of the maximum R_2 over number of cycles for the FE model of critical microstructure of specimen 1.

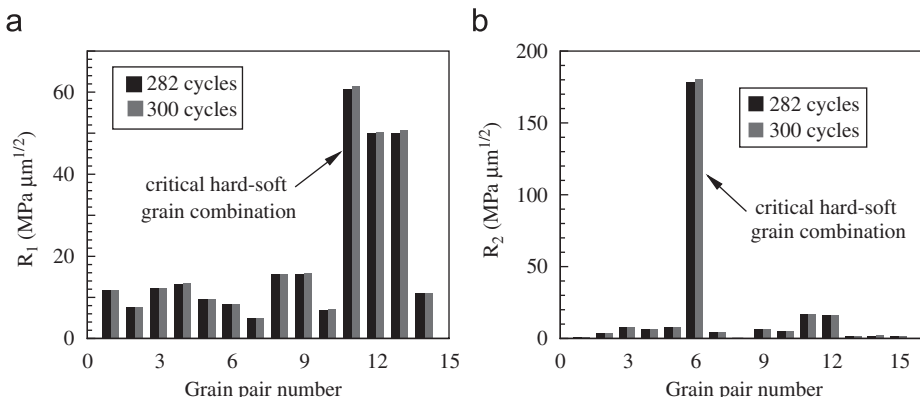


Fig. 14. Histograms of effective crack nucleation variables: (a) R_1 along an X-directed line passing through the hard–soft grain combination with the highest R_1 value, (b) R_2 along an X-directed line passing through the hard–soft grain combination with the highest R_2 value, for the critical microstructure of specimen 1 at 282 and 300 dwell cycles respectively.

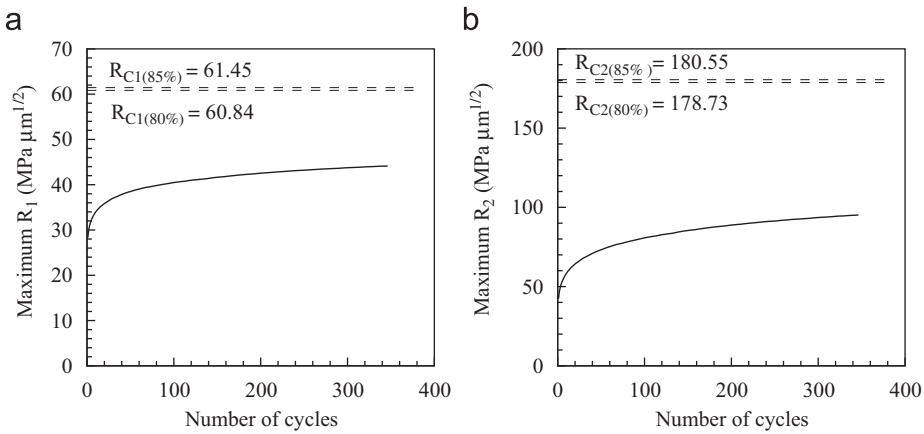


Fig. 15. (a) Evolution of the maximum R_1 over number of cycles for the FE model of non-critical microstructure of specimen 1, (b) evolution of the maximum R_2 over number of cycles for the FE model of non-critical microstructure of specimen 1.

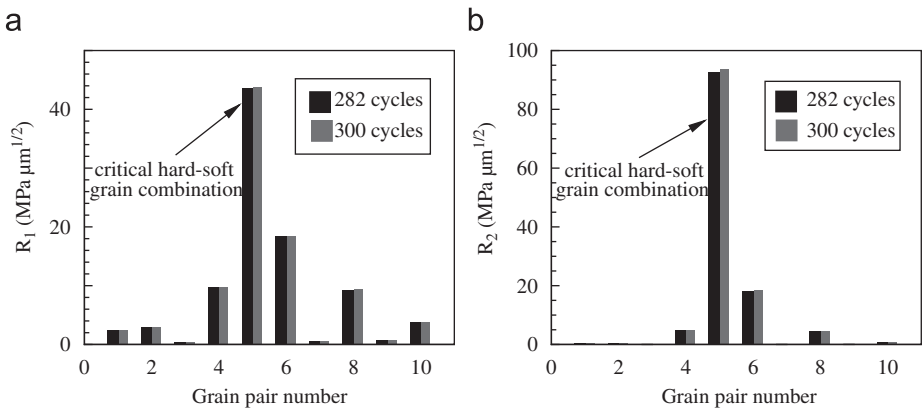


Fig. 16. Histograms of effective nucleation variables: (a) R_1 along an X-directed line passing through the hard-soft grain combination with the highest R_1 value, (b) R_2 along an X-directed line passing through the hard-soft grain combination with the highest R_2 value, corresponding to the non-critical microstructure of specimen 1 at 282 and 300 dwell cycles.

nucleation for the polycrystalline crystal plasticity microstructure, constructed for the non-critical region. This is consistent with experimental observations. In this microstructure the hard-soft grain combination with the highest value of R_1 is the same as that with the highest value of R_2 . Histograms of R_1 and R_2 along an X-directed line passing through this grain pair at 282 and 300 cycles are shown in Fig. 16(a) and (b).

6.2. Predicting crack nucleation in specimens 2 and 3

Statistically equivalent CPFE models of the critical microstructure of specimens 2 and 3 are generated from orientation imaging microscopy scans surrounding primary and secondary cracks in the failed specimens. For specimen 2, crack nucleation is experimentally determined to occur at 530 cycles in Section 3.2. The 2-min CPFE simulation is performed for 663 cycles using loading conditions described in Rokhlin et al. (2005). Fig. 17(a) shows the evolution of the maximum R_1 with cycles, where Eq. (26) is used to estimate c . In this figure the R_1 curve does not intersect the critical values of R_{c1} . Therefore no crack nucleation is predicted within the 663 cycles if Eq. (26) is used. However if Eq. (28) is used to estimate c , the number of cycles to nucleation is predicted as $N_{c2(80\%)} = 534$ and $N_{c2(85\%)} = 567$. These correspond to the locations where the R_2 curve in Fig. 17(b) intersects the critical values of $R_{c2(80\%)}$ and $R_{c2(85\%)}$ respectively. The difference with the experimentally determined value of 530 cycles is 0.72% for 80% of life and 6.93% for 85% of life. This agreement is considered to be excellent.

Finally, the 2-min dwell fatigue problem is simulated for 447 cycles for the critical microstructure of specimen 3. Evolution of the maximum R_1 with the crack length c_1 is plotted in Fig. 17(c). The criterion is not able to predict a crack nucleation for specimen 3 within the 447 cycles, if Eq. (26) is used. However, the evolution of the maximum R_2 using the crack length c_2 in Eq. (28) is plotted in Fig. 17(d). The number of cycles to nucleation are predicted to be $N_{c2(80\%)} = 385$ and $N_{c2(85\%)} = 405$. From Table 1, experimentally this crack is seen to initiate at 380 cycles. The differences in the simulated and

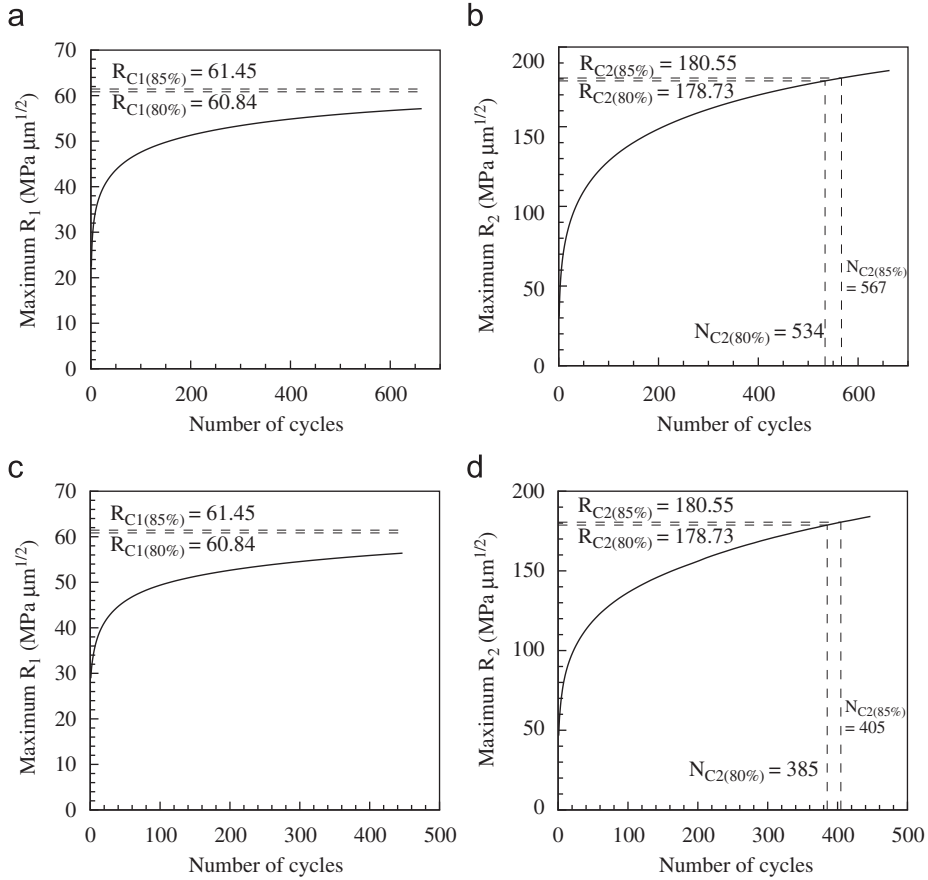


Fig. 17. (a) Evolution of the maximum R_1 over number of cycles for the FE model of critical microstructure of specimen 2, (b) evolution of the maximum R_2 over number of cycles for the FE model of critical microstructure of specimen 2, (c) evolution of the maximum R_1 over number of cycles for the FE model of critical microstructure of specimen 3, (d) evolution of the maximum R_2 over number of cycles for the FE model of critical microstructure of specimen 3.

Table 3

Microstructural features of predicted location of crack nucleation site in dwell fatigue of Ti-6242.

Microstructural parameters	Experiments	Specimen 1	Specimen 2	Specimen 3
θ_c	$\sim 0-30^\circ$	14.5°	36.7°	23.8°
Prismatic Schmid factor	$\sim 0.0-0.1$	0.03	0.16	0.08
Basal Schmid factor	$\sim 0.3-0.45$	0.24	0.47	0.34

experimental results are 1.35% for 80% of life and 6.49% for 85% of life. From these results, it is evident that using Eq. (28) for the crack length results in excellent agreement of the predicted number of cycles to crack nucleation and experimental observations. Results of crack nucleation from the evolution of R_2 are summarized in Table 2. Alternatively, if R_{c2} is calibrated from results on specimen 2, the calibrated value is found to be $R_{c2} = 178.51 \text{ MPa } \mu\text{m}^{1/2}$. Correspondingly, the number of cycles to nucleation for specimen 3 is found to be $N_{c2} = 383$. This corresponds to only a 0.7% difference from the experimentally determined value of 380 cycles.

As an additional validation measure, characteristics of the local microstructure are identified at the crack nucleation sites in the CPFE domain and compared with the corresponding experimental observations made in Sinha et al. (2006b). Results computed with the crack length c_2 and the effective nucleation parameter R_2 are given in Table 3. Specifically, three dominant microstructural characteristics contributing to the crack nucleation process are compared. These are the c -axis orientation (θ_c) and the Schmid factors of the prismatic and basal planes for the hard grain. The simulated predictions are very consistent with the experimental observations in Sinha et al. (2006b). These results prove convincingly the predictive capability of the crack nucleation criterion both in terms of the overall life and location of cracks.

7. Conclusion

This paper develops a novel grain-level crack nucleation criterion for dwell fatigue in polycrystalline titanium alloys. The model utilizes evolving variables that are computed in crystal plasticity finite element (CPFE) simulations of polycrystalline microstructures to construct a criterion that is able to effectively predict the number of cycles to crack nucleation, as well as the characteristics of the local site. The basic idea behind this model is that dislocations piled up against the grain boundary in a soft grain can produce a wedge type micro-crack in an adjacent hard grain. The crack nucleation model include some of the following features:

- Interaction of all active slip systems are accounted for through plastic deformation gradients in the calculation of micro-crack opening.
- Dislocations in the pileup contribute to the wedge crack opening, through the magnitude of plastic deformation gradient and the distance from grain boundary.
- Mixed-mode cracking is considered.
- It is non-local, accounting for stress concentration in the hard grain as well as dislocation pileup in adjacent soft grain.
- Location and direction of the micro-crack are calculated.

A necessary ingredient for this nucleation model is an experimentally validated, rate and size dependent, crystal plasticity FE model for computational modeling of the mechanical response at the level of individual grains. The 3D CPFE models utilize polycrystalline microstructures that have equivalent statistics of morphological and crystallographic characteristics. The computer models are created from failure sites (critical region) and non-failure sites (non-critical regions) of the specimens. Fatigue cracks are observed to nucleate with stress concentration caused by the load shedding phenomenon between adjacent hard and soft grains. The load shedding induced crack nucleation criterion depends on the local stresses in the hard grain as well as the non-local plastic strain gradients in adjacent soft grains. A direct approach is proposed in this paper to evaluate the micro-crack length in the hard grain using the distribution of geometrically necessary dislocations inside a contiguous soft grain. The local effective stress required for crack nucleation is inversely related to the non-local plastic strain gradients in the neighboring soft grain. The proposed crack nucleation model can be reduced to a form similar to the Cottrell–Petch model in the limit, if only one slip plane of edge dislocations is considered.

The critical parameter in the crack nucleation model is calibrated using experimental results of ultrasonic crack monitoring in dwell fatigue experiments. The model is then validated against limited experimental data through predictions of the number of cycles to failure as well as the critical features of the failure site for dwell fatigue experiments. The general agreement with experiments is very satisfactory. In conclusion, the proposed model is adequate for identifying fatigue crack nucleation sites and the corresponding number of cycles in a polycrystalline aggregate. Evolving the cracks for life prediction is still a considerable challenge since appropriate fracture models must be incorporated to propagate the cracks.

Acknowledgements

This work has been supported by the FAA (Grant # DTFA03-01-C-0019, Program Manager: Dr. Joe Wilson), and Air Force Office of Scientific (Grant # FA-9550-09-1-0452, Program Manager: Dr. David Stargel). Computer support by the Ohio Supercomputer Center through grant # PAS813-2 is also acknowledged.

References

- Acharya, A., Beaudoin, A.J., 2000. Grain-size effect in viscoplastic polycrystals at moderate strains. *J. Mech. Phys. Solids* 48, 2213–2230.
- Anahid, M., Chakraborty, P., Joseph, D.S., Ghosh, S., 2009. Wavelet decomposed dual-time scale crystal plasticity FE model for analyzing cyclic deformation induced crack nucleation in polycrystals. *Model. Simul. Mater. Sci. Eng.* 37 (064009).
- Anderson, T.L., 2005. Fracture Mechanics: Fundamentals and Applications. CRC Press.
- Ashby, M.F., 1970. The deformation of plastically non-homogeneous materials. *Philos. Mag.* 21, 399–424.
- Bache, M.R., 2003. A review of dwell sensitive fatigue in titanium alloys: the role of microstructure, texture and operating conditions. *Int. J. Fatigue* 25, 1079–1087.
- Bennett, V., McDowell, D., 2003. Polycrystal orientation distribution effects on microslip in high cycle fatigue. *Int. J. Fatigue* 25, 27–39.
- Bhat, S., Fine, M., 2001. Fatigue crack nucleation in iron and a high strength low alloy steel. *Mater. Sci. Eng. A* 314, 90–96.
- Chu, R., Cai, Z., Li, S., Wang, Z., 2001. Fatigue crack initiation and propagation in an α -iron polycrystals. *Mater. Sci. Eng.* 313, 61–68.
- Coffin, L.F., 1973. Fatigue. *Ann. Rev. Mater. Sci.* 2, 313–348.
- Cottrell, A.H., 1958. Theory of brittle fracture in steel and similar metals. *Trans. Met. Soc. AIME* 212, 192–203.
- Dawson, P., 2000. Computational crystal plasticity. *Int. J. Solids Struct.* 37, 115–130.
- Deka, D., Joseph, D.S., Ghosh, S., Mills, M.J., 2006. Crystal plasticity modeling of deformation and creep in polycrystalline Ti-6242. *Metall. Trans. A* 37A (5), 1371–1388.
- Dunne, F., Rugg, D., 2008. On the mechanisms of fatigue facet nucleation in titanium alloys. *Fatigue Fract. Eng. Mater. Struct.* 31, 949–958.
- Engelen, R.A.B., Geers, M.G.D., Baaijens, F.P.T., 2003. Nonlocal implicit gradient-enhanced elasto-plasticity for the modeling of softening behavior. *Int. J. Plasticity* 19, 403–433.
- Fine, M., Ritchie, R., 1979. Fatigue and Microstructure. American Society for Metals, Metals Park, OH.
- Fleck, N.A., Kang, K.J., Ashby, M.F., 1994. The cyclic properties of engineering materials. *Acta Metall. Mater.* 42, 365–381.

- Ghosh, S., Anahid, M., Chakraborty, P., 2010. Modeling fatigue crack nucleation using crystal plasticity finite element simulations and multi-time scaling. In: Ghosh, S., Dimiduk, D. (Eds.), Computational Methods for Microstructure-Property Relationships. Springer, New York, Dordrecht, Heidelberg, London, pp. 497–554.
- Ghosh, S., Bhandari, Y., Groeber, M., 2008. CAD based reconstruction of three dimensional polycrystalline microstructures from FIB generated serial sections. *J. Comput. Aid. Des.* 40 (3), 293–310.
- Goh, C., McDowell, D., Neu, R., 2006. Plasticity in polycrystalline fretting fatigue contacts. *J. Mech. Phys. Solids* 54, 340–367.
- Goh, C., Neu, R., McDowell, D., 2003. Crystallographic plasticity in fretting of Ti-6Al-4V. *Int. J. Plasticity* 19, 1627–1650.
- Groeber, M., Ghosh, S., Uchic, M.D., Dimiduk, D.M., 2008a. A framework for automated analysis and representation of 3D polycrystalline microstructures, part 1: statistical characterization. *Acta Mater.* 56 (6), 1257–1273.
- Groeber, M., Ghosh, S., Uchic, M.D., Dimiduk, D.M., 2008b. A framework for automated analysis and representation of 3D polycrystalline microstructures, part 2: synthetic structure generation. *Acta Mater.* 56 (6), 1274–1287.
- Hashimoto, T.M., Pereira, M.S., 1996. Fatigue life studies in carbon dual-phase steels. *Int. J. Fatigue* 18 (8), 529–533.
- Hasija, V., Ghosh, S., Mills, M.J., Joseph, D.S., 2003. Modeling deformation and creep in Ti-6Al alloys with experimental validation. *Acta Mater.* 51, 4533–4549.
- Heinz, A., Neumann, P., 1990. Crack initiation during high cycle fatigue of an austenitic steel. *Acta Metall. Mater.* 38 (10), 1933–1940.
- Imam, M.A., Gilmore, C.M., 1979. Room temperature creep of Ti-6Al-4V. *Metall. Trans. A* 10A, 419–425.
- Kim, W., Laird, C., 1978a. Crack nucleation and stage I propagation in high strain fatigue I. Microscopy and interferometric observations. *Acta Metall.* 26 (5), 777–787.
- Kim, W., Laird, C., 1978b. Crack nucleation and stage I propagation in high strain fatigue—II. Mechanism. *Acta Metall.* 26 (5), 789–799.
- Kirane, K., Ghosh, S., 2008. A cold dwell fatigue crack nucleation criterion for polycrystalline Ti-6242 using grain-level crystal plasticity FE model. *Int. J. Fatigue* 30, 2127–2139.
- Kirane, K., Ghosh, S., Groeber, M., Bhattacharjee, A., 2009. Crystal plasticity finite element based grain level crack nucleation criterion for Ti-6242 alloys under dwell loading. *J. Eng. Mater. Technol. ASME* 131, 27–37.
- Laird, C.M., 1976. The fatigue limit of metals. *Mater. Sci. Eng.* 22, 231–236.
- Lim, L., 1987. Surface intergranular cracking in large strain fatigue. *Acta Metall.* 35 (7), 1653–1662.
- Lin, M., Fine, M., Mura, T., 1986. Fatigue crack initiation on slip bands: theory and experiment. *Acta Metall.* 34 (4), 619–628.
- McDowell, D., Dunne, F., 2010. Microstructure-sensitive computational modeling of fatigue crack formation. *Int. Fatigue* 32, 1521–1542.
- Mineur, M., Villechaise, P., Mendez, J., 2000. Influence of the crystalline texture on the fatigue behavior of a 316L austenitic stainless steel. *Mater. Sci. Eng. A* 286, 257–268.
- Morrissey, R., Goh, C., McDowell, D., 2003. Microstructure-scale modeling of HCF deformation. *Mech. Mater.* 35, 295–311.
- Neeraj, T., Hou, D.H., Daehn, G.S., Mills, M.J., 2000. Phenomenological and microstructural analysis of room temperature creep in Titanium alloys. *Acta Mater.* 48, 1225–1238.
- Nye, J.F., 1953. Some geometrical relations in dislocated crystals. *Acta Metall.* 1, 153–162.
- Parvatareddy, H., Dillard, D.A., 1999. Effect of mode-mixity on the fracture toughness of Ti-6Al-4V/FM-5 adhesive joints. *Int. J. Fracture* 96, 215–228.
- Petch, N.J., 1959. In: Averbach, B.L., Felbeck, D.K., Hahn, G.T., Thomas, D.A. (Eds.), *Fracture*. John Wiley, New York, p. 54.
- Rice, J., Tracey, D., 1969. On the ductile enlargement of voids in triaxial stress fields. *J. Mech. Phys. Solids* 17 (3), 201–217.
- Rice, J.R., 1968. A path independent integral and the approximate analysis of strain concentration by notches and cracks. *J. Appl. Mech.* 35, 379–386.
- Rokhlin, S., Kim, J.Y., Zoofan, B., 2005. Unpublished research. The Ohio State University, Columbus, OH.
- Ruiz, G., Pandolfi, A., Ortiz, M., 2001. Three-dimensional cohesive modeling of dynamic mixed mode fracture. *Int. J. Numer. Methods Eng.* 52, 97–120.
- Sinha, S., Ghosh, S., 2006. Modeling cyclic ratcheting based fatigue life of HSLA steels using crystal plasticity FEM simulations and experiments. *Int. J. Fatigue* 28, 1690–1704.
- Sinha, V., Mills, M.J., Williams, J.C., 2006a. Crystallography of fracture facets in a near alpha titanium alloy. *Metall. Trans. A* 37A, 2015–2026.
- Sinha, V., Spowart, J.E., Mills, M.J., Williams, J.C., 2006b. Observations on the faceted initiation site in the dwell-fatigue tested Ti-6242 alloy: crystallographic orientation and size effects. *Metall. Trans. A* 37A, 1507–1518.
- Smith, E., 1966. The formation of a cleavage crack in a crystalline solid—I. *Acta Metall.* 14, 985–989.
- Smith, E., 1979. Dislocations and cracks. In: Nabarro, F.R.N. (Ed.), *Dislocations in Solids*, vol. 4. North-Holland, Amsterdam, The Netherlands, pp. 363–449.
- Stroh, A.N., 1954. The formation of cracks as a result of plastic flow. *Proc. R. Soc. London Ser. A* 223, 404–414.
- Suresh, S., 1998. *Fatigue of Materials*. Cambridge University Press, Cambridge.
- Turkmen, H., Loge, R., Dawson, P., Miller, M., 2003. On the mechanical behavior of AA 7075-T6 during cyclic loading. *Int. J. Fatigue* 25, 267–281.
- Venkataraman, G., Ghosh, S., Mills, M.J., 2007. A size dependent crystal plasticity finite element model for creep and load-shedding in polycrystalline Titanium alloys. *Acta Mater.* 55, 3971–3986.
- Venkataraman, G., Kirane, K., Ghosh, S., 2008. Microstructural parameters affecting creep induced load shedding in Ti-6242 by a size dependent crystal plasticity FE model. *Int. J. Plast.* 24, 428–454.
- Venkataraman, G., Deka, D., Ghosh, S., 2006. Crystal plasticity based FE model for understanding microstructural effects on creep and dwell fatigue in Ti-6242. *ASME J. Eng. Mater. Technol.* 128 (3), 356–365.
- Williams, J.C., 2006. The Evaluation of Cold Dwell Fatigue in Ti-6242. FAA Report Summary. The Ohio State University.
- Xie, C., Ghosh, S., Groeber, M., 2004. Modeling cyclic deformation of HSLA steels using crystal plasticity. *ASME J. Eng. Mater. Technol.* 126, 339–352.
- Yao, Y., Fine, M., Keer, L., 2007. An energy approach to predict fatigue crack propagation in metals and alloys. *Int. J. Fract.* 146, 149–158.
- Zhang, Z., Wang, Z., 2003. Dependence of intergranular fatigue cracking on the interactions of persistent slip bands with grain boundaries. *Acta Mater.* 51 (2), 347–364.